4th Workshop on Metallization for Crystalline Silicon Solar Cells

Aluminum-Silicon interdiffusion in screen printed metal contacts for silicon based solar cells applications

M. Balucani[a],*, L. Serenelli[b], K. Kholostov[a], P. Nenzi[a], M. Miliciani[c], F. Mura[d] M. Izzi[b], M. Tucci[b]

[a]*DIET- Sapienza University of Rome, Via Eudossiana, 18 - 00184 Roma, ITALY*
[b]*ENEA Casaccia Research Centre Rome, Via Anguillarese 301, 00123, ITALY*
[c]*CHIMET SpA Thick film division, via di Pescaiola 74, 52040 Viciomaggio, Arezzo, ITALY*
[d] *SBAI, Sapienza University of Rome, Piazzale Aldo Moro, 5 – 00185 Roma, ITALY*

Abstract

In this work we propose a detailed investigation of the Al – Si interdiffusion that occurs during the firing process of the Al-Si back contact of silicon based solar cells. The investigation is based on high resolution scanning electron microscopy (SEM) and compositional microanalysis with energy dispersive X-Ray microanalysis (EDX). We have found a dependence of Si precipitation in the Al matrix depending on the microstructure of the Al screen printable paste. We suggest a gettering effect promoted by the larger Al particles lying within the Al paste being able to affect the Al paste resistivity, the Al distribution within the BSF region of the solar cell, thus affecting the solar cell performances and finally the Al paste thermal expansion coefficient. Finally we demonstrate that the presence of the glass frit reduces the surface tension and, homogenizes the diffusion process. Reduction of surface tension decreases the internal pressure and increases the Si interdiffusion in Al.

Keywords: silicon diffusion, Al-Si microstrcture, Al-Si back contact, solar cells

* Corresponding author. Tel.: +39-06-44585846; fax: +39-06-44585918.
  E-mail address: balucani@die.uniroma1.it

1. Introduction

The most common technology for p-type based crystalline silicon solar cell manufacturing involves a front phosphorous diffused emitter, passivated by a silicon nitride layer and contacted by a screen printed silver grid, while the back contact is screen printed and fired Al paste. Common screen printable Al pastes are able to form deep and effective industrial Al Back Surface Field (BSF), providing also surface recombination velocity values in the range of a few hundred cm/s and performing a backside segregation gettering of undesired metal content within the silicon network. Nevertheless it is widely known that during the co-firing process needed to form both front and back contacts of the solar cells, the Al and Si interdiffuse each other. Details of this process are still under investigations to improve the BSF, the specific contact resistivity as well as the screen printed Al paste conductivity to enhance the solar cell performance. On the other hand, there is a growing interest on industrially scaled passivated emitter and rear cell structure (PERC) cells [1], because of their higher efficiency potential. In this technology the backside is passivated by an insulating layer (e.g. Al_2O_3, SiN_x, SiO_2 or stacks of them [2-4]) on which some openings are performed by laser ablation, in both holes or continuous rows design [5-6]. Then, even if Aluminum screen printing could be performed as a grid to allow bifacial cells, it is commonly adopted the same back layout as conventional cells, with an extended screen printing of Al, with some silver zones to allow cell interconnections into a module. Even if in this way the screen printing is kept as simple as possible, there are some new requirements for the Al paste, which needs to form a good contact just in the holes or rows, to have a higher conductivity to better transport carriers from contact points to silver tabs, to have a good adhesion on insulating material and to ensure no bowing for the finished cells. Several studies have been carried out on such kind of cells and pastes, especially concerning the filling of insulating layer apertures and the silicon diffusion into Al suitable to avoid the undesired voids formation [7-8]. This last point still needs a deep investigation about the mechanism of Al-Si interdiffusion, and in particular its dependence on the primary paste composition elements: Al particle size and frit presence and composition. Basically the thermodynamic behavior that occurs at the Al-Si interface at equilibrium is described by the Al-Si phase diagram as reviewed in [9]. Explanation of the microstructure formation between screen printed Al pastes and Si only based on the phase diagram, which applies only for conditions close to thermodynamic equilibrium, is quite not easy due to the fast temperature ramp-up and cooling in the industrial solar cell firing process. Indeed, after the firing process, the Al-Si lamellar microstructures, having a volume fraction of the minor phase always higher than 0.25, are commonly found at Al-Si interface [10]. In this work a detailed investigation of the Al-Si interdiffusion that occurs during the firing process, based on high resolution Scanning Electron Microscopy (SEM) and compositional microanalysis with Energy Dispersive X-Ray microanalysis (EDX) is conducted. The content of silicon as also the BSF dependence on the aluminum paste is investigated and explained.

2. Experimental

Six different Al screen printable pastes have been tested, differing one from each other in the particle size distribution and composition. The six pastes were produced as experimental lots by R&D labs of Chimet S.p.A. thick film division, according to the following labels reported in table 1:

Table 1. Aluminum paste distribution: d(0.X)=Y represents the X•10% probability that Al particles diameter are smaller than Y

Description	Min. diameter [μm]	d(0.1) [μm]	d(0.5) [μm]	d(0.9) [μm]	Glass frit	Reference in article
Al X 3027 small particle size	0.955	1.537	2.733	4.746	No	S27
Al X 3028 large particle size	2.512	3.928	5.849	8.703	No	S28
Al X 3029 small particle size	0.955	1.537	2.733	4.746	2% Pb free	S29
Al X 3030 large particle size	2.512	3.928	5.849	8.703	2% Pb free	S30
Al X 3041 **80%** of **S29** and **20%** of **S30**						S41
Al X 3042 **20%** of **S29** and **80%** of **S30**						S42

The small and large particle size powders were supplied from one dealer; therefore they were produced with the same process and same surface characteristics.

Each paste has been tested by measuring: a) the specific contact resistivity with the Si wafer, evaluated with the Transfer Length Method (TLM) technique; b) the conductivity, evaluated with 4 points probe sheet resistance measurement. Solar cells are fabricated using as back contact the six kinds of pastes listed in table 1. For specific contact resistivity measurements several samples have been produced by screen printing 8 patterns for TLM measurements of each paste on 5 Ωcm p-type doped CZ wafers for. All pastes have been printed, dried and fired according the following process parameters: (i) Screen printing: squeegee hardness 70-75 shore, force 7 Kg, speed 100 mm/s, snap off: 0.5 mm. (ii) Screen: 250 mesh stencil screen, wires 36 microns. (iii) Dry: 4 zones IR belt Aurel furnace 250-250-250-250°C, total duration time 2 minutes. (iv) Firing: 3 zones IR belt RTC furnace, settled temperatures 580-640-910 °C speed 50 ipm. To estimate the fired paste conductivity a 4x2 cm^2 area has been fully printed on a similar substrate and using the same parameters as just described. The fired paste layers have been measured by 4 points probe, mapping the whole 4x2 cm^2 area on 6 different points and extracting an average. The bulk conductivities are calculated by considering the paste layer thicknesses.

Solar cells have been fabricated on p-type doped 1 Ωcm 200 μm thick CZ alkaline textured wafers. The front side emitter has been diffused up to 70 Ω/square. The back side electrode has been guaranteed by screen printed Al full coverage and the front side has been ensured by screen printed Ag grid. A co-firing process has been performed in a 3 zones IR belt RTC furnace with settled temperatures of 580-640-950 °C respectively and belt speed of 80 ipm. Samples have been cut from a larger wafer to avoid edge isolation. The solar cells have been measured by means of open circuit voltage (V_{oc}) and Fill Factor (FF) under AM1.5G class A sunlight simulator conditions. Internal Quantum Efficiency (IQE) has been performed in the spectral range between 900 nm and 1200 nm to evaluate the BSF depth. Hall profile measurements have been collected on the Al removed back side of the cell to evaluate the active doping concentration in the BSF region of the cell.

All Al-Si interfaces have been investigated in detail by a FESEM Auriga 405 equipped with Quantax EDX detector for elemental analysis and compositional mapping.

3. Results

Concentration profiles are measured by EDX at different magnification and with two acceleration voltage settings to modify the electron range (i.e. about 1.0 μm @ 10 kV and 0.3 μm @ 5 kV) and consequently the pear-shape of the volume analyzed. SEM images of Al screen printed paste after the firing process at three different magnifications are shown in figure 1a, b, c for samples S27, S28, S29 respectively. The yellow square indicates the area of the average chemical composition measured. In table 2 the amount of Al, Si and oxygen is listed for each of the six samples as deduced from quantitative microanalysis performed at different magnifications and energies.

Table 2. Microanalysis composition of the different samples

| Magnification and Energy	Materials	Sample S27 at.%	1 Sigma	Sample S28 at.%	1 Sigma	Sample S29 at.%	1 Sigma	Sample S30 at.%	1 Sigma	Sample S41 at.%	1 Sigma	Sample S42 at.%	1 Sigma
10000, 10kV	Al	76.24	3.10	68.63	3.04	68.67	3.29	53.87	2.53	68.65	2.54	71.04	3.14
	Si	10.92	0.44	17.69	0.76	15.68	0.73	29.31	1.32	12.70	0.47	11.80	0.52
	O	7.98	0.56	8.48	0.65	10.04	0.81	10.84	0.85	13.87	0.83	11.78	0.86
2500, 10kV	Al	74.90	3.08	62.83	2.73	68.20	3.29	60.87	2.82	68.90	2.57	69.19	3.24
	Si	11.67	0.48	23.46	0.98	15.25	0.72	22.16	0.99	10.71	0.40	13.20	0.61
	O	8.01	0.57	8.62	0.65	10.34	0.83	10.93	0.85	14.88	0.89	11.59	0.90
1000, 5kV	Al	62.55	2.63	49.08	2.10	58.98	2.55	51.27	2.24	63.61	2.58	60.61	2.46
	Si	21.46	0.95	31.68	1.40	19.93	0.90	24.61	1.12	11.42	0.51	16.83	0.73
	O	14.09	0.97	17.10	1.18	17.42	1.20	19.38	1.34	22.35	1.39	20.07	1.27
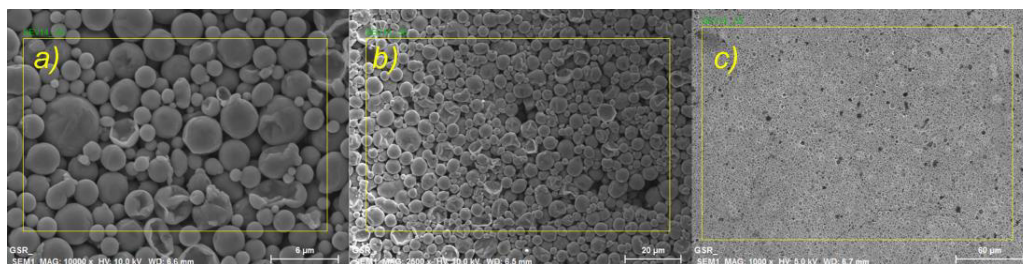
Fig. 1. (a) Sample S27; (b) Sample S28; (c) Sample S29.

The Si compositional mappings of sample S42 and S41 are shown in figure 2a and 2b respectively. A Focused Ion Beam (FIB) cross-section of compositional mapping and quantitative analysis of sample S28 are shown in figure 3.
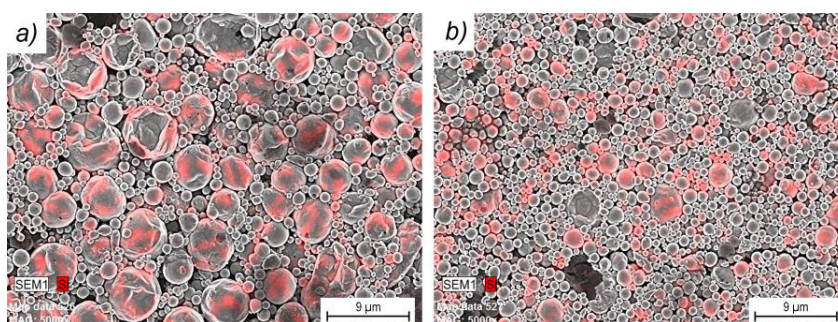

Fig. 2. Silicon compositional mapping of (a) sample S42 and (b) sample S41. Magnification of the images are the same.

The electrical characteristics of the different samples are given in table 3, with the specific contact resistivity (ρ_c) of the Al-Si contact, the Al paste resistivity (ρ) after firing, the open circuit voltage (V_{oc}), the normalized fill factor (FF) with respect to sample S28 and the BSF thickness.

Table 3. Electrical properties of samples (n.m.=not measured)

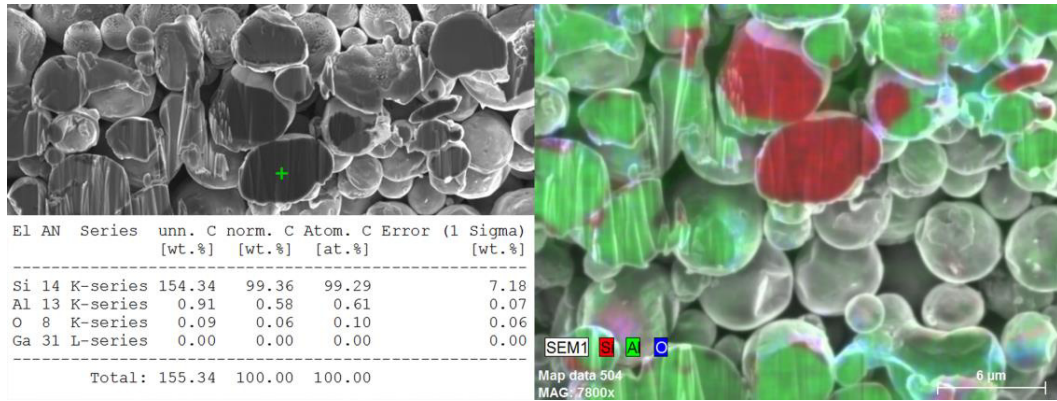| Sample	ρ_c	ρ	V_{oc}	FF	BSF
	[mΩcm^2]	[$\mu\Omega$cm]	[mV]	normalized to S28	[μm]
S27	47.3	32.3	614	0.938	6.1
S28	57.8	26.2	620	1.000	5.1
S29	53.8	28.4	625	0.949	5.9
S30	58.7	23.8	628	0.912	4.9
S41	n.m.	49.3	622	0.946	5.0
S42	n.m.	27.7	613	0.914	5.3

Fig. 3. Silicon, aluminium and oxygen compositional mapping of sample S28 (left); quantitative analysis of a big ball filled by silicon (right)

4. Discussion

We have found that the relevant mechanism of the Si dispersion within Al is strongly correlated to the Al particle dimensions. This behavior, opposite to what asserted in ref. [11], occurs because interfaces become extremely important in the early stages of phase transformation where the two phases (i.e. Al and Si) are influenced by the pressure difference modifying the solubility (interdiffusion coefficient) that depends on the curvature radius of the two phases interfaces. This effect can be explained just as a soap bubble exerts an extra pressure on its contents [12] and as given by the well-known Laplace–Young equation that was proven to be valid in the phenomenological description of internal pressure and surface tension of nanoparticles with dimension down to 2 nm [13]:

$$\Delta P = \frac{2\gamma}{r} \tag{1}$$

where γ and r are respectively the surface tension and radius of the Al sphere.

Moreover the Al-Si interaction strongly depends on the presence of the glass frit inside the Al screen printable paste. The glass frit influences the Al-Si interaction modifying the surface tension of the molten liquid of Al. Materials like Bismuth, Calcium and Magnesium, at low concentration (i.e. Bi~0.3 at%, Ca~1.5 at%, Mg~3.5 at%) are able to almost half the surface tension of liquid Al [14, 15, 16]. Furthermore, these elements, even at a low concentration, weaken or thin the surface oxide film surrounding the Al particles. In particular Bi is able to disrupt the Al_2O_3 oxide [17], while Si does not reduce surface tension but improves the fluidity [18].

Our investigation of the Al-Si begins considering the case of glass frit absence in the Al paste, as for the sample S27-S28. During the thermal heating process, the interdiffusion of Si into Al starts at approximately 300 °C and increases reaching its maximum (i.e. 1.5 at%) at the eutectic temperature (T_{eut} = 577 °C). Considering that the particles dimension of the Al paste have a radius (r) greater than 100 nm (i.e.: S27 r ≥ 477 nm, S28 r ≥ 1250 nm), the melting temperature of such microspheres can be considered equivalent to that of bulk aluminum and not reduced as happens for smaller metallic particles [19]. It must be recalled that Si diffusion in Al is faster than Al in Si, therefore Al-Si solid particles appear before the eutectic temperature is reached.

Storaska and Howe [20] observed that Al-Si particles contain a single crystal α-Al matrix with multiple Si precipitates embedded within. Since the Al-Si particle is Al rich and Al has a greater affinity for oxygen than silicon, the amorphous oxide, covering the Al-Si sphere, contains mainly Al and O. Analyzing diffraction patterns, Storaska and Howe, found prominent α-Al matrix reflections in solid Al-Si particles, as well as weaker Si precipitate reflections and some Al-silicate (Al-Si-O) reflections. The weak Al-silicate diffraction spots indicate the presence of small nano-crystallites of Al-silicate in, or adjacent to, the oxide shell. The Si precipitates are

observed to migrate at the oxide-matrix interface. The solid Al-Si particles that for simplicity can be considered like spheres start to melt as soon as the eutectic temperature is exceeded. The melting process, observed by transmission electron microscopy (TEM), starts near the Si particles present at the oxide interface, with a liquid sheath appearing and thickening as the temperature increases [21]. The sheath continues to thicken as the temperature rises and the remaining small, solid core rapidly melts. Similar behavior was observed also for pure Al particles [22].

At liquid state the Al-Si particles develop two internal pressure contributions. The first is due to volume expansion of Al-Si spherical particle, where the volume of a spherical particle with the radius *r* changes at a rate of:

$$\frac{dV}{dr} = 4\pi r^2 = 3\frac{V}{r}$$

(2)

Rearranging eq. (2), it shows that the radial strain is one-third of the fractional volume change:

$$\frac{dr}{r} = \left(\frac{1}{3}\right)\frac{dV}{V}$$

(3)

Since Si is present as a second phase in the particles, the fractional volume-change associated with melting of an Al-Si alloy can be estimated by:

$$\frac{\Delta V_{melt}}{V_0} = \frac{\left(X_{Si}V_{Si}^l + X_{Al}V_{Al}^l\right) - \left(X_{Si}V_{Si}^S + X_{Al}V_{Al}^S\right)}{\left(X_{Si}V_{Si}^S + X_{Al}V_{Al}^S\right)}$$

(4)

where X_{Si}, V_{Si}^l, V_{Si}^S, X_{Al}, V_{Al}^l, and V_{Al}^S are the mole fractions and liquid and solid volume of Si and Al respectively, and V_0 is the initial volume. Considering, as a first approximation, the density value of Si and Al as $\rho_{Sisolid} = 2.33$, $\rho_{Siliquid} = 2.54$, $\rho_{Alsolid} = 2.70$ and $\rho_{Alliquid} = 2.375$ all in g/cm³, at the eutectic concentration of 12.2 at% Al-Si alloy, the volume change (eq. 4) is 10.21%. This produces a corresponding radial strain (eq. 3) of 3.4%, which is also equivalent to the tangential strain in the oxide shell, since the radius and circumference are linearly related. Storaska and Howe measured a linear change in diameter on melting that was approximately 3%. This is in reasonable agreement with the value calculated above and is a large strain compared to the measured 0.2% critical tensile-strain of aluminum-oxide [23, 24]. Following these data, the volume expansion induces a very strong stress on the thin oxide leading to Al-Si particle explosion. In practice more than 90% of the oxide survives during melting [20] suggesting that a kind of stress-relief mechanism should be present that allows the oxide to relieve the tangential stress. Observations by TEM and also MD (molecular dynamic) simulations, revealed that if there exists a non-uniform oxide layer, during melting such region undergoes a further thinning and a through-thickness crack develops in the oxide of the molten particle allowing the liquid to spur through the crack decreasing the internal pressure [20, 25, 26]. The influence of curvature radius on the internal pressure due to the volume expansions can be determined by using thin-walled pressure vessel mechanism. The maximum internal pressure of the Al-Si liquid phase due to the stressed oxide-shell can be determined from the following force-balance equation [27]:

$$P_I = P_S\left(\frac{2t}{r}\right)$$

(5)

where P_I is the internal pressure on the Al-Si liquid, P_S is the pressure in the oxide shell, *t* is the oxide thickness and *r* the radius of the Al-Si particle. Thus for a given internal pressure, as the radius decreases, the pressure of the oxide shell must increase in order to allow the force-balance. This clearly shows that a smaller Al-Si particle experiences higher pressure and tends to start the stress-relief mechanism before that in the bigger particles. This stress-relief mechanism is not observed for Al-Si particles with dimensions lower than about 40nm (r = 20nm) [26]. Considering that the stress-relief mechanism due to oxide thinning seems to be a creep mechanism, at nano-

scale the creep mechanism is quite reduced [28], therefore it makes no sense to use Al paste from Al powder having nano-scale dimensions.

The described mechanism reasonably explains why Al paste, with smaller particles, shows higher Al concentration at the Al-Si interface with respect to that with bigger particles. The Al concentration increment improves the BSF depth and enhances the peek of doping profile of the BSF region. Smaller Al particles are available and more Al spheres will undergo the stress-relief mechanism increasing the Al concentration at the silicon surface inducing also a decrease in the specific contact resistivity as can be seen in table 3. As predicted, the BSF depth values reported in table 3 show that smaller Al particles produce a deeper BSF region.
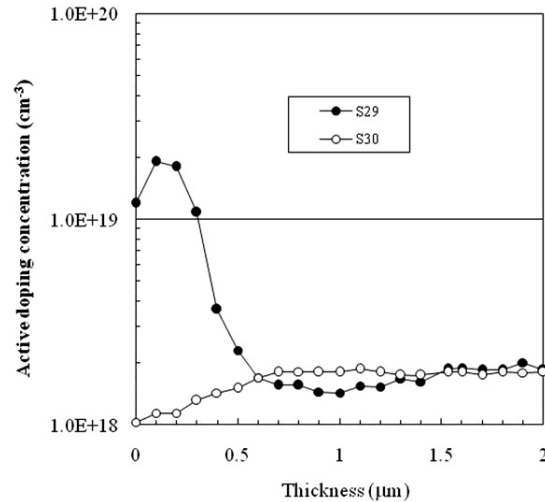

Fig. 4. Active doping profile of BSF region of sample S29 and S30

The increment in peak has been confirmed by the comparison of active doping profiles of the BSF region measured on sample S29 and S30 reported in figure 4 and listed in table 3. Consequently a benefit occurs on the V_{oc} values of the cell, due to a built-in voltage increment on the overall cell structure.

The second internal pressure contribution that the Al-Si particle develops, and that does not influence the oxide shell stress, is the pressure given from eq. (1). The total pressure (eq. (1) + eq. (5)) inside the liquid Al-Si particles affects the interfusion of Si into Al. As shown in ref. [29], the diffusion coefficient is proportional to the total pressure reciprocal inside the Al-Si particles. At nanometer scale, eq. (1) can reach pressures of GPa magnitude [30]. Thus, the pressure can affect the Si interdiffusion coefficient if is in the range between 15 to 20 atm or higher.

The calculated pressure for different particle dimensions, taking into account that the surface tension of molten Al is $\gamma = 0.865$ N/m [14], is reported in table 4 as for sample S27 and S28. Then a radius dimension reduction of a factor of two halves the diffusion coefficient of Si inside Al. Analyzing in detail all the samples, we have found that the microstructure is always lamellar, independently of where the observation is taken (i.e.: Al-Si interface) as shown in figure 5, or figure 6 within the Al matrix.

Table 4. Pressure due to eq (1) inside Al-Si particle

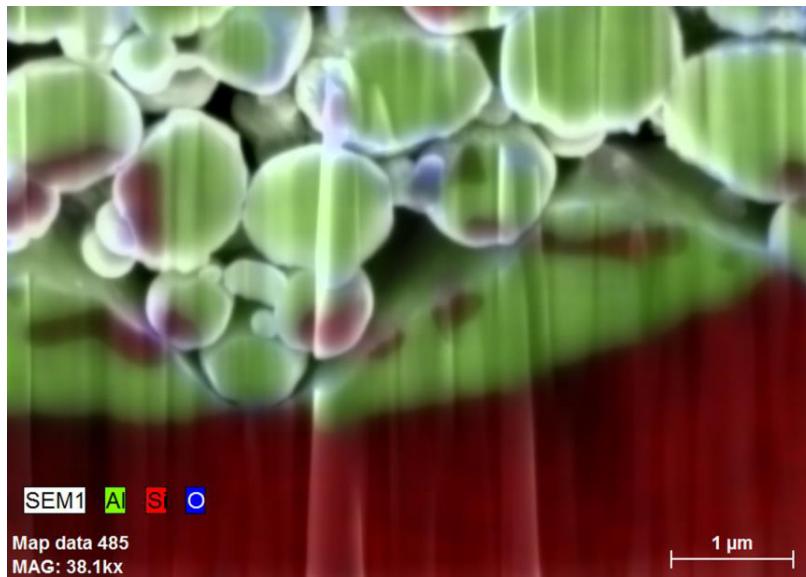| Sample	Min. diameter	P	d(0.1)	P	d(0.5)	P	d(0.9)	P	Glass frit
	[μm]	[atm]	[μm]	[atm]	[μm]	[atm]	[μm]	[atm]	
S27	0.955	36.2	1.537	22.5	2.733	12.66	4.746	7.3	No
S28	2.512	13.8	3.928	8.8	5.849	5.9	8.703	4.0	No

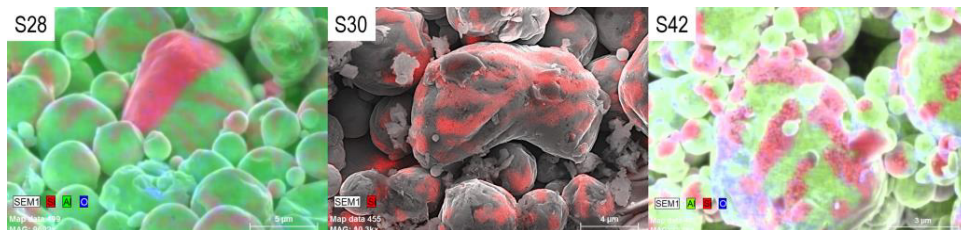Fig. 5. Silicon compositional mapping of sample S41 close the silicon interface

Fig. 6. Silicon compositional mapping of sample S30 and S42 in the middle of the Al matrix, S28 on top of the Al-matrix surface

The lamellar structures are always formed from rich Al phase (i.e.: concentration higher than 98 at%) and Si rich phase (i.e.: higher than 99 at%) and the silicon mainly tends to segregate to the interface region. As already found in ref. [31], we also experimentally found strong presence of silicon at the interface, thus suggesting that Al oxidation at the interface may strongly be influenced by the Si segregation. Both Si and Al can be easily oxidized because of their low equilibrium oxygen partial pressure. A competition between Al oxidation and Si segregation at the interface can then be supposed as possible inhibition mechanism for the Al_2O_3 step formation for a pure Al-Al_2O_3 interface [31], as shown is figure 7 where no silicon segregation is found.
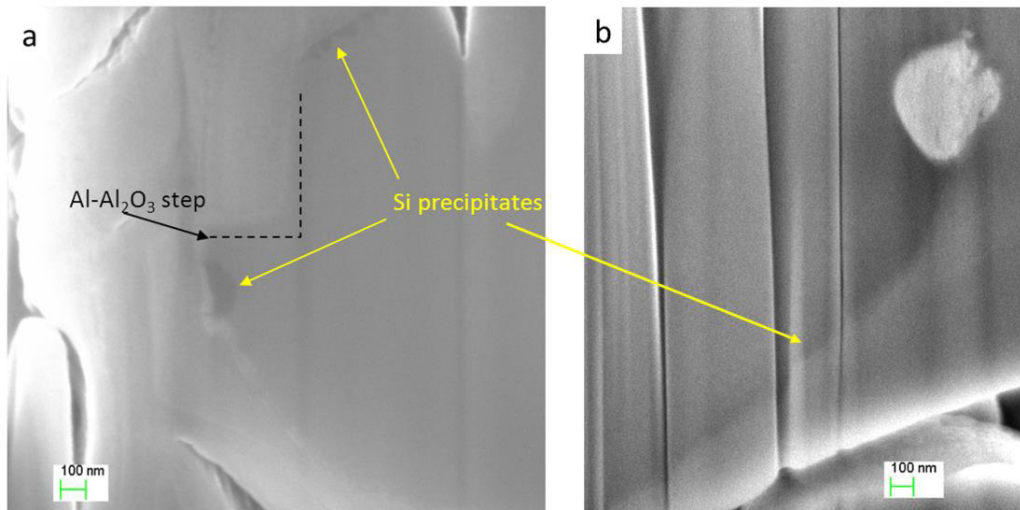
Fig. 7. (a) Al-Al$_2$O$_3$ abrupt step where no silicon precipitation is present (b) silicon precipitate (darker area) along the Al-Al$_2$O$_3$ interface

Furthermore, looking at table 2, it is evident that as the electron range decreases, decreasing the energy (i.e. 5 kV) the concentration of silicon and oxides increases. This is because the pear-shape of SEM investigation penetrates less, thus more information from the surface can be gained, indicating a greater oxide amount due to the Al$_2$O$_3$ interface and greater amount of Si due to the Si precipitation at the Al$_2$O$_3$ interface.

The Al particle dimensions influence the Si interdiffusion. As can be seen from table 2, samples with smaller Al particles (i.e. S27 and S29) shows lower content of Si with respect to samples with bigger particles (i.e. S28 and S30). Moreover, from figure 2 it can be observed that the bigger sphere getters a great amount of Si due to the lower internal pressure meanwhile is in the liquid state, thus reducing the Si diffusion elsewhere. Also from figure 2b it is possible to see that many small particles have Si inclusion even not as pronounced as in case of bigger spheres. We can conclude that only big Al particles can be totally filled with Si and this is easily explained by the low internal pressure of the big particles with respect to the small ones. This gettering effect also modifies the thermal expansion coefficient (TEC). Indeed, as an example, the TEC of pure Al is 24 ppm/°C, the TEC of Al-12at%Si is 20 ppm/°C and the TEC of Al-27at%Si is 16 ppm/°C [32].

Now, taking into account that: (i) silicon precipitates at the Al$_2$O$_3$ interface; (ii) bigger particles getter Si leaving the smaller particles with less silicon inside, we can focus on Al paste bulk resistivity values taken, after firing, as listed in table 3. Taking into account that the current mainly flows through a small curvature radius, it preferentially passes through the small Al-Si particles and if these particles have an amount of Si precipitates these last increase the percolation resistance influencing the bulk resistivity. On the other hand we can deduce that the Al paste bulk resistivity is lower when a silicon gettering mechanism is effective as in case of big Al particles. This can be seen from table 3 comparing sample S28 with respect to S27, S30 with respect to S29 and S42 with respect to S41.

The presence of the glass frit reduces the surface tension and homogenizes the diffusion process. Reduction of surface tension decreases the internal pressure and increases the Si interdiffusion in Al. As an example Bi, at a concentration of only 0.3 at% reduces the surface tension by a factor of two (i.e. $\gamma = 0.5$ N/m [14]). This effect is similar to doubling the curvature radius of the Al-Si particles and in presence of the glass frit it is possible to see also small particles fully filled with Si, as shown in figure 8 for sample S41. In turn, Al paste S27 nowhere shows small particles fully filled with silicon.
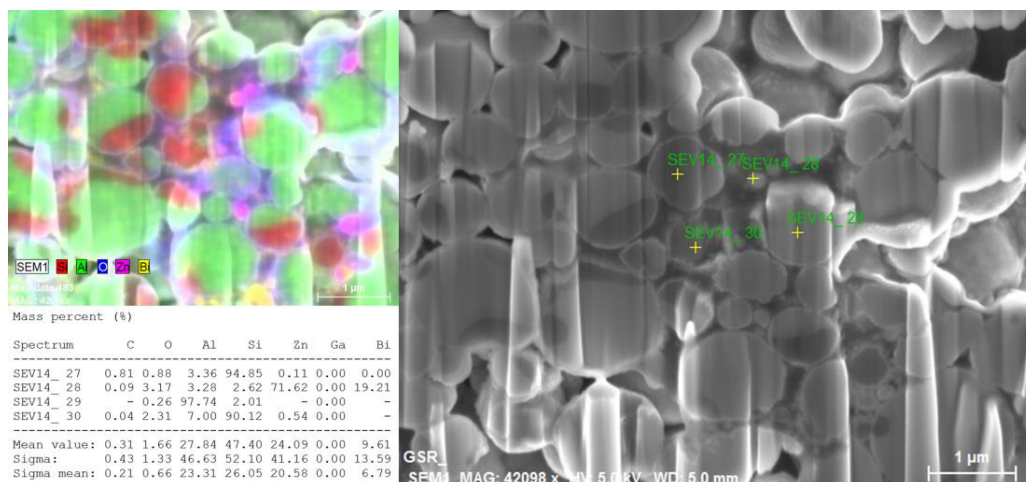
Fig. 8. Upper left compositional mapping of sample S41 and quantitative analysis at different points

5. Conclusion

Using SEM pictures and detailed EDX investigation at the Al-Si interface we have found that the relevant mechanism of the silicon dispersion within Aluminum is strongly related to the Al particle dimensions. Only big Al particles can be totally filled with Si and this is explained by the low internal pressure of the larger particles with respect to the small ones. This gettering effect promoted by the larger Al particles affects the Al paste resistivity as well as the Al distribution within the BSF region of the solar cell thus affecting the cell performance. Moreover the Al-Si interdiffusion also modifies the thermal expansion coefficient. We have also found that the lamellar structures are always formed from a Al rich phase and a Si rich phase and that the silicon mainly tends to segregate at the interface region.

Finally we have demonstrated that the presence of the glass frit reduces the surface tension and, homogenizes the diffusion process. Reduction of surface tension decreases the internal pressure and increases the Si interdiffusion in Al.

References

[1] Blakers AW, Wang A, Milne AM, Zhao J, Green MA. 22.8% efficient silicon solar cell. *Appl Phys Lett* 1989;**55**(13):1363-5.

[2] Veith B, Dullweber T, Siebert M, Kranz C, Werner F, Harder N-P, Schmidt J, Roos BFP, Dippell T, Brendel R. Comparison of ICP-AlOx and ALD-Al2O3 Layers for the Rear Surface Passivation of C-Si Solar Cells. *Energy Procedia* 2012;**27**:379–84.

[3] Urrejola E, Petres R, Glatz-Reichenbach J, Peter K, Wefringhaus E, Plagwitz H, Schubert G. High Efficiency Industrial PERC Solar Cells with all PECVD-Based Rear Surface Passivation. *Proceedings of the 26th European Photovoltaic Solar Energy Conference and Exhibition,* 2011, p 2233–5.

[4] Schmidt J, Kerr M, Cuevas A. Surface passivation of silicon solar cells using plasma-enhanced chemical-vapour-deposited SiN films and thin thermal SiO2/plasma SiN stacks. *Semicond Sci Technol* 2001;**16**:164–70.

[5] Jaffrennou P, Uruena de Castro A, Das J, Penaud J, Moors M, Rothschild A, Lombardet B, Szlufcik J. Laser Ablation of SiO2/SiNx and AlOx/SiNx Back Side Passivation Stacks for Advanced Cell Architectures. *Proceedings of the 26th European Photovoltaic Solar Energy Conference and Exhibition*, 2011, p. 2180–3.

[6] Zielke D, Petermann JH, Werner F, Veith B, Brendel R, Schmidt J. 21.7 % Efficient PERC Solar Cells with AlOx Tunneling Layer. *Proceedings of the 26th European Photovoltaic Solar Energy Conference and Exhibition*, 2011, p. 1115-9.

[7] Urrejola E, Peter K, Plagwitz H, Schubert G. Silicon diffusion in aluminum for rear passivated solar cells. *Appl Phys Lett* 2011;**98**(15):153508.

[8] Urrejola E. Aluminum-Silicon Contact Formation Through Narrow Dielectric Openings. Dr. rer. nat. Thesis:2012. Available online http://nbn-resolving.de/urn:nbn:de:bsz:352-194453.

[9] Murray JL, McAlister AJ. The Al-Si (Aluminum-Silicon) System. *Bulletin of Alloy Phase Diagrams* 1984;**5**(1):74-84.

[10] Kurz W, Fisher DJ, *Fundamental of Solidification Vol. 1*, Trans Tech Publications; 1998.

[11] Rajendran RG, Liang L, Roelofs MG. Silicon-free aluminium paste composition for forming an aluminium back electrode with large silicon particles. Patent:2012; US 2012/0318343A1.

[12] Porter DA, Easterling KE, *Phase Transformations in Metals and Alloys 2nd Edition*, Chapman & Hall; 1992.

[13] Hawa T, Zachariah MR. Internal pressure and surface tension of bare hydrogen coated silicon nanoparticles. *Journal of Chemical Physics* 2004;**121**(18):9043-9.

[14] Miyoshi T, Hara S, Mukai T, Higashi K. Development of a Cloaed Cell Aluminum Alloy Foam with Enhancement of the Compressive Strength. *Materials Transactions* 2001;**42**(10):2118-23.

[15] Hashim J, Looney L, Hashmi MSJ. The wettability of SiC particles by molten aluminium alloy. *Journal of Materials Processing Technology* 2001;**119**(1-3):324-8.

[16] Eustathopoulos N, Joud JC, Desre P, Hicter JM. The wetting of carbon by aluminium and aluminium alloys. *Journal of Materials Science* 1974;**9**(8):1233-42.

[17] Papworth A, Fox P. The disruption of oxide defects within aluminium alloy castings by the addition of bismuth. *Materials Letters* 1998;**35**(3-4):202-6.

[18] Van Horn KR, editor. *Aluminum vol 1*, New York:American Society for Metals; 1967, p. 179.

[19] Hasegawa M, Watabe M and Hoshino K. A theory of melting in metallic small particles. *J Phys F: Metal Phys* 1980;**10**(4):619-35.

[20] Storaska GA and Howe JM. In-situ transmission electron microscopy investigation of surface-oxide, stress-relief mechanisms during melting of sub-micrometer Al–Si alloy particles. *Materials Science and Engineering:A* 2004;**368**(1-2):183-90.

[21] Storaska GA. In-Situ TEM Investigation of the Solid-Liquid Interface in Sub-Micron Al-Si Alloy Particles. M.S. Thesis:2001, University of Virginia, Charlottesville, Virginia.

[22] Arai S, Tsukimoto S, Saka H. In Situ Transmission Electron Microscope Observation of Melting of Aluminum Particles. *Microscopy and Microanalysis* 1998;**4**(03):264-8.

[23] Schütze M. Deformation and Cracking Behavior of Protective Oxide Scales on Heat-Resistant Steels under Tensile Strain. *Oxidation of Metals* 1985;**24**(3/4):199-232.

[24] Schütze M. Mechanical aspects of high-temperature oxidation. *Corrosion Science* 1993;**35**(5-8):955-63.

[25] Puri P Yang V. Thermo-mechanical behavior of nano aluminum particles with oxide layers during melting. *Journal of Nanoparticle Research* 2010;**12**(8):2989-3002.

[26] Levita VI, Pantoya ML, Chauhan G, Rivero I. Effect of the alumina shell on the melting temperature depression for nano-aluminum particles. *The Journal of Physics Chemistry C* 2009;**113**(32):14088-96.

[27] Hertzberg RW. *Deformation and Fracture Mechanics of Engineering Materials, 4th edition*, New York:Wiley; 1996, p. 11, 22, 45, 233.

[28] Mavoori H. Significantly enhanced creep resistance in low-melting-point solders through nanoscale oxide dispersions. *Appl Phys Lett* 1998;**73**(16):2290-2.

[29] Kapoor K, Kumari R, Dass N, Kumar R. A model for the pressure dependence of diffusion in condensed matter. *Pramana Journal of physics* 2006;**67**(3):541-6.

[30] Johnson E. The Elusive Liquid-Solid Interface, *Science* 2002;**296**(5567):477-8.

[31] Montesa CM, Shibata N, Choi S-Y, Tonomura H, Akiyama K, Kuromitsu Y, Ikuhara Y. High-Resolution Transmission Electron Microscopy Observation of Liquid-Phase Bonded Aluminum/Sapphire Interfaces. *Materials Transactions* 2009;**50**(5):1037-40.

[32] Hidnert P, Krider HS, Thermal Expansion of Aluminum and Some Aluminum Alloys, *Journal of Research of the National Bureau of Standards* 1952;**48**(3):209-20.